Ni *et al.*
Chinese Journal of Mechanical Engineering (2024) 37:51
https://doi.org/10.1186/s10033-024-01033-5

Chinese Journal of Mechanical Engineering

ORIGINAL ARTICLE **Open Access**

Theoretical Modeling and Surface Roughness Prediction of Microtextured Surfaces in Ultrasonic Vibration-Assisted Milling

Chenbing Ni[1*], Junjie Zhu[1], Youqiang Wang[1], Dejian Liu[1], Xuezhao Wang[1] and Lida Zhu[2*]

Abstract

Textured surfaces with certain micro/nano structures have been proven to possess some advanced functions, such as reducing friction, improving wear and increasing wettability. Accurate prediction of micro/nano surface textures is of great significance for the design, fabrication and application of functional textured surfaces. In this paper, based on the kinematic analysis of cutter teeth, the discretization of ultrasonic machining process, transformation method of coordinate systems and the cubic spline data interpolation, an integrated theoretical model was established to characterize the distribution and geometric features of micro textures on the surfaces machined by different types of ultrasonic vibration-assisted milling (UVAM). Based on the theoretical model, the effect of key process parameters (vibration directions, vibration dimensions, cutting parameters and vibration parameters) on tool trajectories and microtextured surface morphology in UVAM is investigated. Besides, the effect of phase difference on the elliptical shape in 2D/3D ultrasonic elliptical vibration-assisted milling (UEVAM) was analyzed. Compared to conventional numerical models, the method of the cubic spline data interpolation is applied to the simulation of microtextured surface morphology in UVAM, which is more suitable for characterizing the morphological features of microtextured surfaces than traditional methods due to the presence of numerous micro textures. The prediction of surface roughness indicates that the magnitude of ultrasonic amplitude in *z*-direction should be strictly limited in 1D rotary UVAM, 2D and 3D UEVAM due to the unfavorable effect of axial ultrasonic vibration on the surface quality. This study can provide theoretical guidance for the design and fabrication of microtextured surfaces in UVAM.

Keywords Theoretical modeling, Microtextured surface, Ultrasonic vibration-assisted milling, Cubic spline interpolation, Surface roughness

1 Introduction

In the last few decades, the application of difficult-to-machine material parts in aerospace, military, and biomedical fields has grown rapidly due to their outstanding physical and mechanical properties. However, these special physicochemical properties of difficult-to-machine materials (such as high strength, high hardness, etc.) lead to common problems in conventional machining, such as low machining efficiency, low material removal rate, high surface roughness, rapid tool wear, etc. Due to the significant technical advantages over conventional machining, ultrasonic machining (UM) technology has been successfully applied to high-performance machining of difficult-to-machine materials such as titanium alloys, superalloys, high-performance ceramics and composite materials [1]. In comparison to simple smooth surfaces obtained by conventional machining, uniform texture with complex

---

*Correspondence:
Chenbing Ni
nichenbing@126.com
Lida Zhu
neulidazhu@163.com
[1] School of Mechanical and Automotive Engineering, Qingdao University of Technology, Qingdao 266525, China
[2] School of Mechanical Engineering and Automation, Northeastern University, Shenyang 110819, China

micro/nano structures is a prominent morphological feature of surfaces machined by UM [2]. Therefore, to a certain extent, UM technology can be classified as a branch of surface texture preparation technology, which enables the fabrication of surface textures with high efficiency and cost effective [3].

1.1 Advanced Properties of Microtextured Surfaces

Textured surfaces with suitable micro/nano structures have been proven to possess some advanced functional properties at the surface/interface of mechanical parts, such as bearings [4, 5], gears [6], seals [7], cutting tools [8, 9]. Obviously, textured surfaces perform different functional behaviors in different applications, such as reducing friction, improving wear and increasing wettability. Currently, surface texture manufacturing technologies mainly include laser processing, electrochemical machining, chemical etching, electric discharge machining, photo-etching and ultrasonic vibration-assisted machining [10], which are attracting widespread attention from scholars. Compared with other surface texture technologies, ultrasonic machining has distinct advantages of simultaneously forming the part, improving the surface quality, increasing the surface strength, and texturing the surface in a one-time operation. In addition, ultrasonic machining technology can be combined with 4- and 5-axis machine tools to realize the fabrication of surface textures on complex curved surfaces [11].

Based on a kinematic model and a pressing model, Shen and Tao [12, 13] studied the formation mechanism of fish-scale weave surfaces in feed-direction vibration-assisted milling (UVAM) process, and investigated the frictional properties of microtextured surfaces under boundary lubrication conditions. Shen and Tao concluded that the micro textures with proper pattern contributes to improve the absorption and storage capacity of lubricating oil, thus forming a strong oil film. Amini et al. [14] experimentally studied the effect of different vibration modes (1D linear, 2D elliptical and 3D elliptical) on the tribological behavior of textured surfaces machined by ultrasonic vibration-assisted turning (UVAT). Compared to normal turned surfaces, the average friction coefficients of textured surfaces generated by 1D linear, 2D elliptical and 3D elliptical UVAT showed a maximum improvement of 13%, 18% and 21%, respectively. Besides, the water droplet contact angle of the surfaces generated by conventional turning, 1D linear, 2D elliptical and 3D elliptical UVAT are 55.9°, 46.1°, 38.9° and 33.3°, respectively [15]. Guo et al. [16] reported the improved anisotropic wettability of textured surfaces with graded microstructure, which was produced by ultrasonic elliptical vibration cutting (EVC). Because of the anisotropic wettability caused by hierarchical miniature structures, the water contact angles along the vertical direction on the surface are always greater than those along the parallel direction. Based on the analysis of microstructure and wettability of rotational ultrasonic textured surfaces, Xu et al. [17] attributed the enhanced anisotropic hydrophilic surfaces to the combination of increased surface area and directional surface textures. Convex grating is a kind of special diffraction grating in which the intensity distribution of diffracted light is precisely adjusted through the depression and elevation structure of the surfaces. Chen et al. [18] successfully fabricated mid-infrared relief gratings on silicon and aluminum materials by using a controllable special-shaped vibration cutting method.

1.2 Modeling of Microtextured Surface Morphology

The accurate prediction of microtextured topography is of great significance for the design, fabrication and application of functional textured surfaces. In general, the prediction of microtextured surfaces can be obtained by extending the prediction method of common machined surfaces. Based on the *Z*-map model and the discretization of cutting motion including the tool motion, cutting-tool edges and workpiece, Liu et al. [19] developed a comprehensive geometrical simulation system to describe the characteristics of ball-end milling surfaces. By considering the dynamic vibrations of the tool caused by the regenerative chatter, Sun et al. [20] developed an analytical to predict the surface topography formed by robotic milling. Sajjady et al. [18] proposed an algorithm to simulate the topography of microtextured surfaces in ultrasonic vibration assisted turning (UVAT). The results indicated that the texture topography derived from the simulation algorithm matched well with the experimental results. Liu et al. [21] established a theoretical model to describe the geometry and distribution of micro-dimpled textures on the surfaces generated by radial UVAT. According to the moving trajectory model and cutting process model of a single abrasive grain, Jiang et al. [22] studied the formation mechanism of surface textures and developed a theoretical model of microtextured surfaces in ultrasonic vibration-assisted grinding (UVAG). Jiang et al. concluded that the proposed theoretical model could accurately characterize the topographical features of textured surfaces. On the basis of abrasive grain-workpiece contact rate and neural networks of genetic algorithms, Yang et al. [23] developed the prediction models of surface topography and roughness in tangential ultrasonic vibration-assisted grinding (UVAG). Compared with continuous cutting in conventional machining, the motion trajectories of the tool teeth are not equal to the cutting trajectory due to the intermittent cutting mechanism in UM. Based on the analysis of separate cutting process and tool-tip motion trajectories in UVAM, Zhu et al. [24, 25] investigated the formation mechanism of textured surface and the influence of surface textures on frictional properties of machined surfaces. Lu et al. [26] investigated the formation mechanism and the interference effect of surface textures in ultrasonic vibration-assisted end milling and peripheral milling. Through the analysis of the contact and separation behavior between the tool and workpiece, Qin et al. [27] theoretically studied the generation mechanism and developed a prediction model of microtextured surfaces in longitudinal-torsional UVAM.

In this study, based on the analysis of tool trajectories, the discretization of cutting process and the transformation of coordinate systems, an integrated theoretical model was proposed to characterize the morphological features and to evaluate the surface roughness of microtextured surfaced machined by 1D, 2D elliptical and 3D elliptical UVAM. Compared to conventional numerical models, the method of the cubic spline data interpolation is more suitable for characterizing the morphological features of microtextured surfaces than traditional methods due to the presence of numerous micro textures. Finally, based on the analysis of elliptical shapes, tool-tip trajectories and microtextured surface topography features, some significant conclusions closely related to UVAM process have been drawn.

2 Theoretical Modeling of Microtextured Surfaces in UVAM

2.1 Kinematics Analysis of Cutter Teeth

As shown in Figure 1, ultrasonic excitation with micron-level amplitudes is usually superimposed on the tool or workpiece. Both application methods, with their unique advantages, have been proven to significantly improve the machinability of difficult-to-machine materials. Depending on the dimensionality of applied ultrasonic vibrations, UM can be divided into one-dimensional (1D), planar (2D) elliptical and spatial (3D) elliptical vibration-assisted techniques.

The relative motion trajectories between the tool and workpiece play a crucial role in determining the machined surface topography [28]. In UVAM, the tool-workpiece relative motion trajectories are mainly composed of the rotational movement of the machine spindle, the feed motion of the workpiece and the external ultrasonic vibrations. Thus, the trajectories of the tool tip can be expressed as Eq. (1):

$$\begin{cases} x = x_r + x_f + x_v, \\ y = y_r + y_f + y_v, \\ z = z_v, \end{cases} \tag{1}$$

where x_r and y_r denote the rotary motion displacement of the tool in x and y directions, respectively. x_f and y_f indicate the feed displacement of the workpiece along x and y directions, respectively. x_v, y_v and z_v represent the ultrasonic vibration along x, y and z directions, respectively.

The rotational motion displacement of the tooth i can be represented as Eq. (2):

$$\begin{cases} x_{ri} = R\cos(\omega_r t - \dfrac{2\pi z_i}{N_z}) + a, \\ y_{ri} = R\sin(\omega_r t - \dfrac{2\pi z_i}{N_z}) + b, \end{cases} \tag{2}$$

where R is the tool radius, ω_r is the angular speed of the rotating tool, N_z is the number of tool teeth, $z_i = 0, 1, ..., N_z$, and (a, b) is the coordinate value of the tool center.

The feed displacement of the workpiece in milling can be written as Eq. (3):

$$\begin{cases} x_f = v_{fx}t, \\ y_f = v_{fy}t, \end{cases} \tag{3}$$

where v_{fx} and v_{fx} represent the feed rate of the workpiece in x and y directions, respectively.

The ultrasonic harmonic vibrations applied in different directions can be given as Eq. (4):

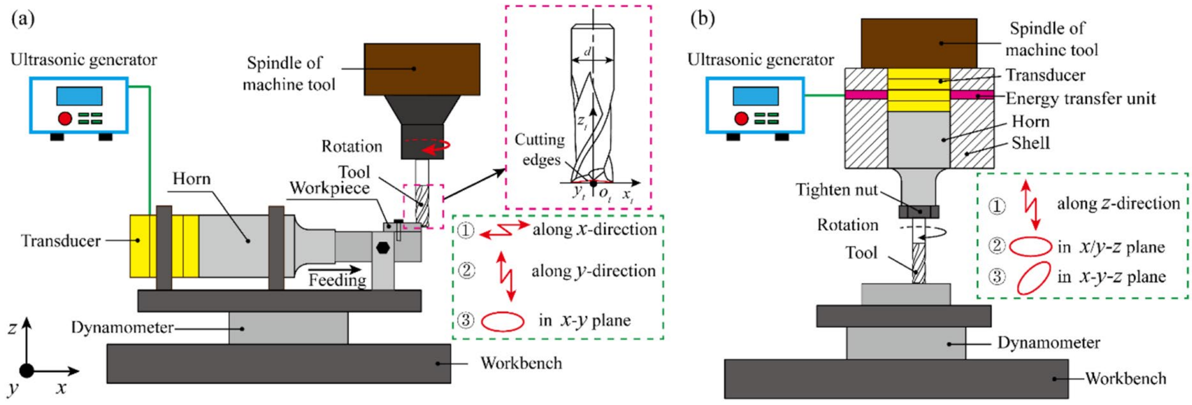

Figure 1 Schematic of different types of UVAM system: Ultrasonic vibration applied to (**a**) the workpiece and (**b**) the tool

$$\begin{cases} x_v = A_x \sin(2\pi ft + \theta_1), \\ y_v = A_y \sin(2\pi ft + \theta_2), \\ z_v = A_z \sin(2\pi ft + \theta_3), \end{cases} \tag{4}$$

where A, f and θ denote the amplitude, frequency and initial phase of ultrasonic vibration, respectively.

Finally, based on Eqs. (1)–(4), the tool motion trajectories in different types of UVAM methods can be written uniformly as Eq. (5):

$$f(x_i, y_i, z_i) = \begin{cases} x_i = R\cos(\omega_r t - \dfrac{2\pi z_i}{N_z}) + v_{fx} t + A_x \sin(2\pi ft + \theta_1), \\ y_i = R\sin(\omega_r t - \dfrac{2\pi z_i}{N_z}) + v_{fy} t + A_y \sin(2\pi ft + \theta_2), \\ z_i = A_z \sin(2\pi ft + \theta_3). \end{cases} \tag{5}$$

2.2 Transformation of the Coordinate Systems

As illustrated in Figure 2, the coordinate systems consist of 5 sub-coordinate systems, namely (1) the workpiece coordinate system O_W-$X_WY_WZ_W$, (2) machine tool spindle coordinate system O_M-$X_MY_MZ_M$, (3) machine tool spindle transition coordinate system O_m-$X_mY_mZ_m$, (4) tool coordinate system O_T-$X_TY_TZ_T$ and (5) tool rotation coordinate system O_t-$X_tY_tZ_t$. The different coordinate systems can be obtained by translation and rotation transformations. Specifically, the coordinate system O_t-$X_tY_tZ_t$ and O_m-$X_mY_mZ_m$ can be transformed into the coordinate system O_T-$X_TY_TZ_T$ and O_M-$X_MY_MZ_M$ through rotation operations, respectively. And the coordinate system O_T-$X_TY_TZ_T$ and O_M-$X_MY_MZ_M$ can be transformed into the coordinate system O_m-$X_mY_mZ_m$ and O_W-$X_WY_WZ_W$ by translation operations, respectively.

According to the transformation theory of the coordinate systems, the translation and rotation transformation matrices are expressed as Eqs. (6) and (7), respectively.

$$T_{translation} = \begin{bmatrix} 1 & 0 & 0 & x_0 \\ 0 & 1 & 0 & y_0 \\ 0 & 0 & 1 & z_0 \\ 0 & 0 & 0 & 1 \end{bmatrix}, \tag{6}$$

$$T_{rotation} = \begin{bmatrix} \cos\alpha & \sin\alpha & 0 & 0 \\ -\sin\alpha & \cos\alpha & 0 & 0 \\ 0 & 0 & 1 & 0 \\ 0 & 0 & 0 & 1 \end{bmatrix}, \tag{7}$$

where $[x_0, y_0, z_0]$ denotes the position of the origin of the old coordinate system in the new coordinate system in translation operation. And α represents the relative rotation angle between the old coordinate system and new coordinate system in the rotation transformation.

In milling, the origin of coordinate system O_M-$X_MY_MZ_M$ is dynamically changing with respect to that of coordinate system O_W-$X_WY_WZ_W$. Therefore, according to the principle of relative motion, the relative displacement between coordinate system O_M-$X_MY_MZ_M$ and O_W-$X_WY_WZ_W$ consists of the initial displacement, the feed motion displacement, the ultrasonic vibration displacement in UVAM. The position of the coordinate origin of coordinate system O_M-$X_MY_MZ_M$ in coordinate system O_W-$X_WY_WZ_W$ can be written as Eq. (8):

$$\begin{cases} x_{W0} = x_{W0'} + v_{fx} t + A_x \sin(2\pi ft + \theta), \\ y_{W0} = y_{W0'} + v_{fy} t + A_y \sin(2\pi ft + \theta), \\ z_{W0} = z_{W0'} + A_z \sin(2\pi ft + \theta), \end{cases} \tag{8}$$

where $(x_{W0}{}', y_{W0}{}', z_{W0}{}')$ represents the initial coordinate of the origin of O_M-$X_MY_MZ_M$ in O_W-$X_WY_WZ_W$ system.

According to the analysis of tool motion trajectories in UVAM and the theory of coordinate system transformation, the cutting trajectories in the workpiece coordinate system O_W-$X_WY_WZ_W$ can be obtained as Eq. (9) through a series of rotational and translational transformations.

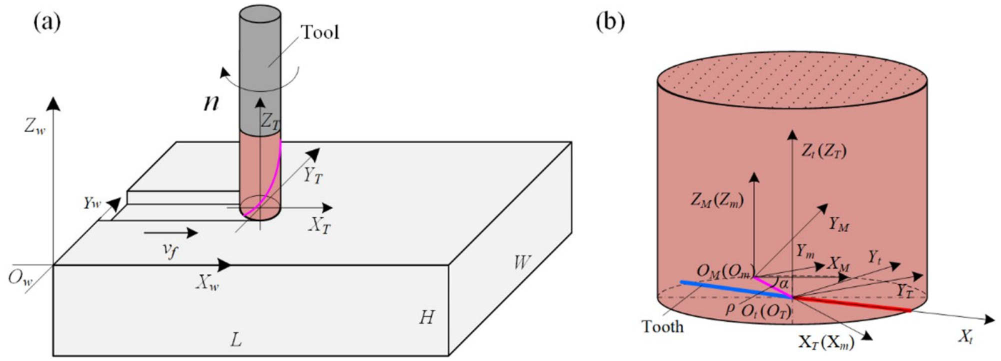

Figure 2 Illustration of coordinate system transformation in end milling: (**a**) End milling operation, (**b**) Sub-coordinate systems

$$\begin{bmatrix} x_W \\ y_W \\ z_W \\ 1 \end{bmatrix} = [T_{WM}][T_{MM'}][T_{M'T}][T_{Tt}] \begin{bmatrix} x_t \\ y_t \\ z_t \\ 1 \end{bmatrix} = \begin{bmatrix} \cos(\lambda+\alpha)x_t + \sin(\lambda+\alpha)y_t + \cos\lambda x_{M0'} + \sin\lambda y_{M0'} + x_{W0} \\ -(\sin(\lambda+\alpha)x_t + \cos(\lambda+\alpha)y_t - \sin\lambda x_{M0'} + \cos\lambda y_{M0'} + y_{W0} \\ z_t + z_{M0'} + z_{W0} \\ 1 \end{bmatrix}, \quad (9)$$

where

$$\boldsymbol{T_{Tt}} = \begin{bmatrix} \cos\alpha & \sin\alpha & 0 & 0 \\ -\sin\alpha & \cos\alpha & 0 & 0 \\ 0 & 0 & 1 & 0 \\ 0 & 0 & 0 & 1 \end{bmatrix}.$$

[$\boldsymbol{T_{Tt}}$] represents the rotational transformation from tool rotation coordinate system O_t-$X_tY_tZ_t$ to tool coordinate system O_T-$X_TY_TZ_T$, and α indicates the rotation angle of the tool.

$$\boldsymbol{T_{M'T}} = \begin{bmatrix} 1 & 0 & 0 & x_{M0'} \\ 0 & 1 & 0 & y_{M0'} \\ 0 & 0 & 1 & z_{M0'} \\ 0 & 0 & 0 & 1 \end{bmatrix}.$$

[$\boldsymbol{T_{M'T}}$] denotes the translational transformation from tool coordinate system O_T-$X_TY_TZ_T$ to the spindle transition coordinate system $O_{M'}$-$X_{M'}Y_{M'}Z_{M'}$, and ($x_{M0'}$, $y_{M0'}$, $z_{M0'}$) indicates the position of the origin of O_T-$X_TY_TZ_T$ system in the $O_{M'}$-$X_{M'}Y_{M'}Z_{M'}$ system.

$$\boldsymbol{T_{MM'}} = \begin{bmatrix} \cos\lambda & \sin\lambda & 0 & 0 \\ -\sin\lambda & \cos\lambda & 0 & 0 \\ 0 & 0 & 1 & 0 \\ 0 & 0 & 0 & 1 \end{bmatrix}.$$

[$\boldsymbol{T_{MM'}}$] represents the rotational transformation from the spindle transition coordinate system $O_{M'}$-$X_{M'}Y_{M'}Z_{M'}$ to the spindle coordinate system O_M-$X_MY_MZ_M$, and λ indicates the rotation angle of the coordinate system $O_{M'}$-$X_{M'}Y_{M'}Z_{M'}$ relative to the coordinate system O_M-$X_MY_MZ_M$.

$$\boldsymbol{T_{WM}} = \begin{bmatrix} 1 & 0 & 0 & x_{W0} \\ 0 & 1 & 0 & y_{W0} \\ 0 & 0 & 1 & z_{W0} \\ 0 & 0 & 0 & 1 \end{bmatrix}.$$

[$\boldsymbol{T_{WM}}$] denotes the translational transformation from the spindle coordinate system O_M-$X_MY_MZ_M$ to the workpiece coordinate system O_W-$X_WY_WZ_W$, and (x_{W0}, y_{W0}, z_{W0}) indicates the position of the origin of the coordinate system O_M-$X_MY_MZ_M$ in the coordinate system O_W-$X_WY_WZ_W$.

2.3 Discretization of UVAM Cutting Process

2.3.1 Discretization of Cutting Edges

The geometric features of end cutting edges are of great significance for the residual profile of machined surfaces in end milling. Figure 3 illustrates the geometric model of a two-flute end mill, in which the coordinate system O_t-$X_tY_tZ_t$ takes the axis of the tool as the z-axis and the line connecting the tool tips as the x-axis. As shown in Figure 3(b), assume that the radius of the tool is R, the secondary declination of the tool is k', and the corner radius is r. Thus, the geometric equation of end cutting edges can be expressed as a piecewise function, which is composed of a linear and circular equations. According to the geometric relationship as shown in the enlarged view, the geometric equation of end cutting edges can be presented as Eq. (10).

$$y = \begin{cases} -x\tan(-1)^i k' + \tan k'(R - r - r\sin k') + r(1-\cos k'),\ x \in (0, R-l), \\ -\sqrt{r^2 - \left[x - (-1)^i(R-x)\right]^2} + r,\ x \in (R-l, R), \end{cases} \quad (10)$$

where i indicates the sequence number of end cutting edge, $i = 0$ or 1 for a two-flute end mill, and $|l| = r(1+\sin k')$.

The cutting edges are discretized into a series of edge microelements dx_t to facilitate the calculation of cutting

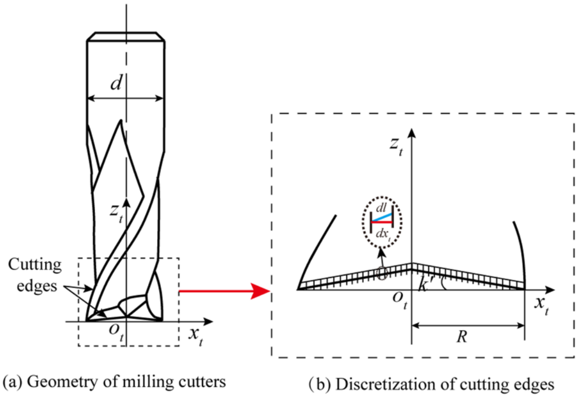

(a) Geometry of milling cutters (b) Discretization of cutting edges

Figure 3 Geometric configuration and discretization of cutting edges trajectories, shown in Figure 3(c). First, according to the geometric Eq. (10) of the end cutting edges, the coordinates of cutting-edge microelements in the tool rotation coordinate system O_t-$X_tY_tZ_t$ can be determined. Second, through rotation and translation transformations, the coordinates of the cutting-edge microelements in the workpiece coordinate system O_w-$X_wY_wZ_w$ can be calculated to determine cutting trajectories. In particular, to ensure the accuracy of the simulation results, the discrete length of the cutting edge dx_t should be smaller than the discrete length of the workpiece surface dx_w. In this paper, the discrete length of the cutting edge is 1/2 of the discrete length of the workpiece.

2.3.2 Discretization of the Workpiece Surface

As shown in Figure 4, the surface of the workpiece to be machined is discretized into a series of matrix grids along the x and y directions, where the length of the discretized microelements is dx_w=dy_w=d. To ensure the simulation efficiency, the height of the workpiece model Lz is slightly larger than the depth of cut. As illustrated in Figure 4(b), the x and y coordinates of each grid point in the workpiece coordinate system can be determined based on the number of rows (i), columns (j) and cell dimensions (d). After the rotation and translation transformations, the position of the cutting-edge microelement dl may be located at grid intersections, grid lines and grid interiors. When the point p on the cutting edge is located on the grid line or inside the grid, the position of the point p can be approximated to the nearest grid point since the size d of the discrete grid on the workpiece surface is small enough. Thus, the position of the point $p(i, j)$ can be approximated as Eq. (11),

$$\begin{cases} i = round(l/d) + 1, \\ j = round(m/d) + 1, \end{cases} \tag{11}$$

where l and m denote the horizontal and vertical coordinates of point p in the workpiece coordinate system, respectively. The *round* function means rounding the value.

The discretization of cutting time is the operation of transforming continuous cutting into intermittent cutting. The total cutting time is closely related to the length of the machining area and the feed rate. It is required that the maximum movement distance of the cutting-edge microelement dx_t in the cutting time microelement dt is less than the length of the grid d. In vertical milling, the maximum cutting speed occurs at the end point of the cutting edges. Therefore, the cutting time microelement dt satisfies Eq. (12):

$$dt \leq \frac{d}{R\omega_r}, \tag{12}$$

where ω_r is the tool rotation angular frequency.

2.3.3 Simulation Procedure of Microtextured Surface Topography

The remapping principle of the tool profile movement is employed to simulate the microtextured surface topography in UVAM, as shown in Figure 5. In machining, although factors such as tool performance, workpiece material, machine tool accuracy and lubrication conditions will have a certain impact on the machined surface morphology, the morphology of the machined surfaces mainly depends on the geometric profile features and motion trajectories of the cutting edges. As given in

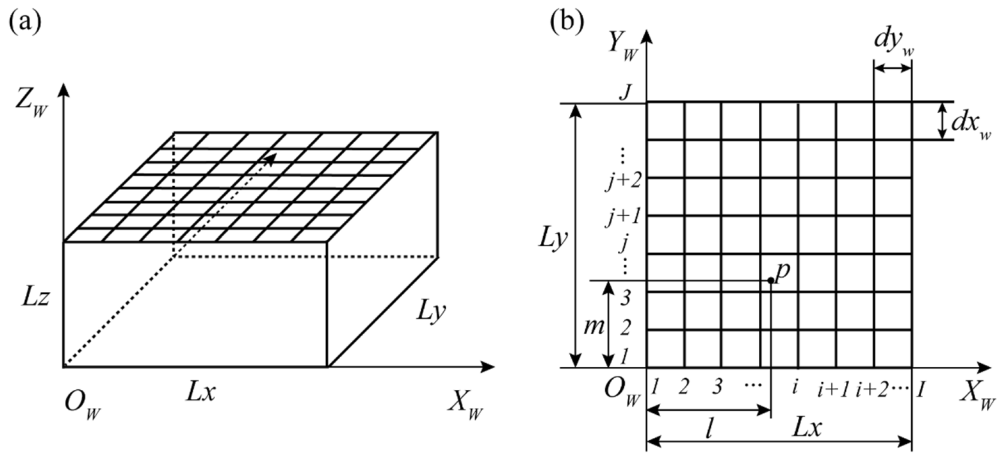

Figure 4 Discretization of the workpiece surface: **a** Surface of workpiece to be machined, **b** Schematic of discrete grids

Figure 5(b), if the ordinate z_w of the discrete point $p(x_w, y_w, z_w)$ transformed into O_w-$X_wY_wZ_w$ system is lower than the ordinate z' of the residual contour at the current position, the ordinate z_w of the discrete point is used to replace the ordinate z' at the current position. This indicates that the discrete cutting-edge cuts into the workpiece. Otherwise, it means that the discrete cutting edge does not effectively cut into the workpiece material. Therefore, the residual contour on the machined surface topography is determined by the lowest coordinate z_w of the swept discrete points at the current position. According to the coordinate transformations of discrete cutting edges and the remapping principle of the tool profile movement, the simulation flow chart of machined surface morphology in UVAM is illustrated in Figure 6.

2.4 Cubic Spline Data Interpolation

In this study, considering the presence of numerous microtextures, the method of cubic spline data interpolation is employed to smooth the discrete data in surface morphology simulation. The piecewise interpolation method is usually used in interpolation to avoid Runge-Kutta phenomenon. As illustrated in Figure 7, the spline curve can be described as a cubic equation in each segment. Thus, $S_i(x)$ is a cubic polynomial of x in each subinterval $[x_i, x_{i+1}]$. The cubic spline function can be expressed as Eq. (13):

$$S_i(x) = a_i + b_ix + c_ix^2 + d_ix^3, \tag{13}$$

where a_i, b_i, c_i and d_i are the undetermined coefficients.

2.5 Effect of Phase Difference of Simple Harmonic Vibrations on the Elliptical Shape

2.5.1 *Elliptical Shape in Plane*

In 2D and 3D ultrasonic machining, the phase difference of ultrasonic vibrations is a determining factor affecting the elliptical shape. And the elliptical shape or trajectory is the dominant factor affecting the morphology and quality of microtextured surfaces. Thus, the effect of phase difference of simple harmonic vibrations on the elliptical shape will be discussed in this section.

The simple harmonic vibrations with ultrasonic frequency in the plane can be expressed as Eq. (14):

$$\begin{cases} x = A_1\cos(\omega t + \varphi_1), \\ y = A_2\cos(\omega t + \varphi_2). \end{cases} \tag{14}$$

Eliminate the variable t by combining two simple harmonic vibrations, thus, Eqs. (15), (16) and (17) can be derived.

$$\begin{cases} \dfrac{x}{A_1}\cos\varphi_2 - \dfrac{y}{A_2}\cos\varphi_1 = \sin\omega t \cdot \sin(\varphi_2 - \varphi_1), \\ \dfrac{x}{A_1}\sin\varphi_2 - \dfrac{y}{A_2}\sin\varphi_1 = \cos\omega t \cdot \sin(\varphi_2 - \varphi_1), \end{cases} \tag{15}$$

$$\frac{x^2}{A_1^2} + \frac{y^2}{A_2^2} - \frac{2xy}{A_1A_2}\cos(\varphi_2 - \varphi_1) = \sin^2(\varphi_2 - \varphi_1), \tag{16}$$

$$\begin{cases} y = \pm\dfrac{A_1}{A_2}x,\ \varphi_2 - \varphi_1 = n\pi\ (n = 0, \pm1, \pm2, \ldots), \\ \dfrac{x^2}{A_1^2} + \dfrac{y^2}{A_2^2} = 1,\ \varphi_2 - \varphi_1 = n\pi + \dfrac{\pi}{2}\ (n = 0, \pm1, \pm2, \ldots), \\ \dfrac{x^2}{A_1^2} + \dfrac{y^2}{A_2^2} - \dfrac{2xy}{A_1A_2}\cos(\varphi_2 - \varphi_1) = \sin^2(\varphi_2 - \varphi_1),\ \text{other}. \end{cases} \tag{17}$$

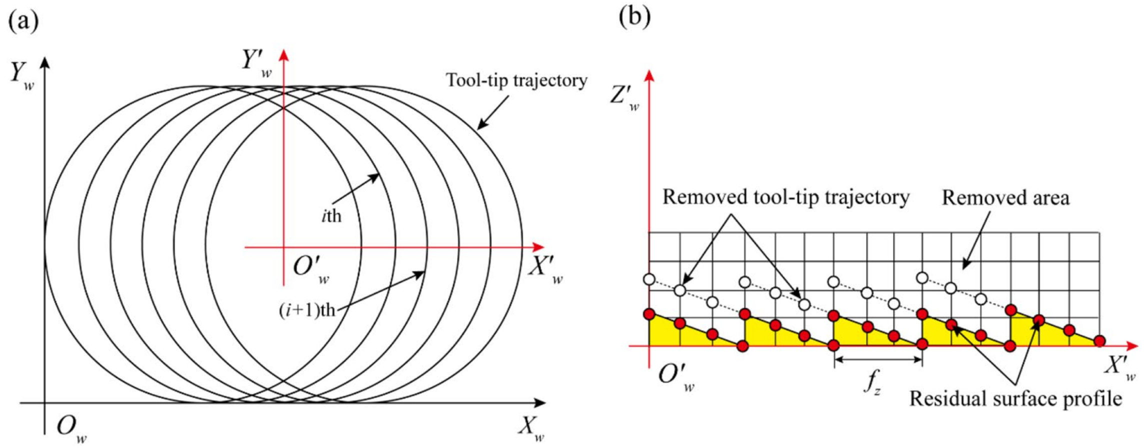

Figure 5 Simulation principle of machined surface topography: **a** Tooth trochoid trajectories in milling, **b** Illustration of machined surface morphology formation

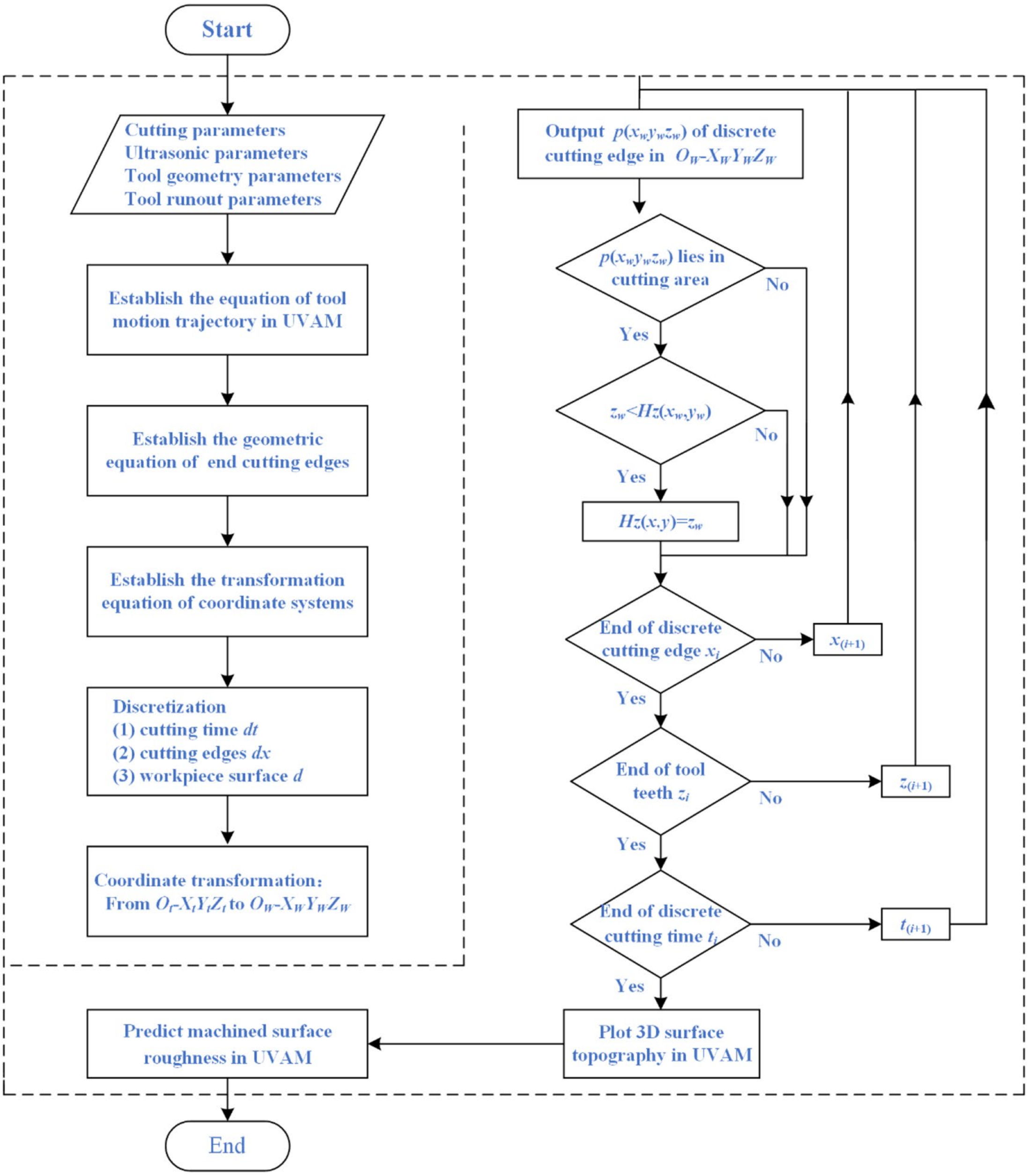

Figure 6 Simulation flow chart of machined surface morphology in UVAM

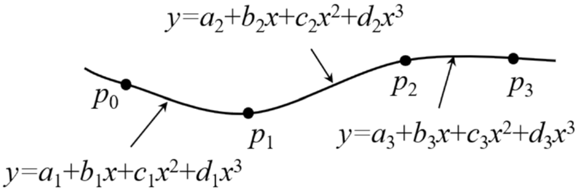

Figure 7 Illustration of cubic spline interpolation

According to Eq. (17), the effect of phase difference of simple harmonic vibrations on the elliptical shape is illustrated in Figure 8. When the phase difference is an integer multiple of π, the coupled trajectory of simple harmonic vibrations is a straight line. When the phase difference is an integer multiple of π, the coupling trajectory of simple harmonic vibrations is a straight line. The coupling trajectory of simple harmonic vibrations is a regular ellipse when the phase difference is an odd multiple of $\pi/2$. In addition, when the phase difference is other values, the coupling trajectory of simple harmonic vibrations is oblique ellipse.

2.5.2 *Elliptical Shape in Space*

Similarly, the simple harmonic vibrations in space can be expressed as Eq. (18):

$$\begin{cases} x = A_1\cos(\omega t + \varphi_1), \\ y = A_2\cos(\omega t + \varphi_2), \\ z = A_3\cos(\omega t + \varphi_3). \end{cases} \tag{18}$$

Then, eliminate the variable t by combining the simple harmonic vibrations, thus, Eq. (19) can be obtained.

$$\frac{2x^2}{A_1^2} + \frac{y^2}{A_2^2} + \frac{z^2}{A_3^2} - \frac{2xy}{A_1A_2}\cos(\varphi_2 - \varphi_1) - \frac{2xz}{A_1A_3}\cos(\varphi_3 - \varphi_1) = \sin^2(\varphi_2 - \varphi_1) + \sin^2(\varphi_3 - \varphi_1). \tag{19}$$

When φ_2–φ_1=90°, Eq. (20) can be obtained:

$$\frac{x^2}{A_1^2} + \frac{y^2}{A_2^2} + \frac{x^2}{A_1^2} + \frac{z^2}{A_3^2} - \frac{2xz}{A_1A_3}\cos(\varphi_3 - \varphi_1) = 1 + \sin^2(\varphi_3 - \varphi_1). \tag{20}$$

Therefore, by adjusting the phase difference of $\Delta=\varphi_3 - \varphi_1$, elliptical trajectories with different attitudes can be obtained in space, as shown in Figure 9.

3 Results and Discussion

3.1 Analysis of Tool-Tip Trajectory in UVAM

3.1.1 *Effect of Vibration Direction and Process Parameters on Tool-Tip Trajectory*

According to Eq. (5), the tool tip trajectory with ultrasonic vibration applied in different directions can be obtained. The simulation parameters are the tool radius d = 8 mm, spindle speed N = 600 r/min, feed rate f = 8 μm/z, ultrasonic frequency f = 20 kHz and ultrasonic amplitude A=10 μm. As shown in Figure 10(a), under the action of spindle rotation motion and workpiece feed motion, the movement trajectory of the tool tip in conventional milling (CM) is a typical hypocycloid. Since the material removal mechanism is dominated by continuous cutting in CM, the motion trajectory of the cutter teeth is equal to the cutting trajectory. As illustrated in Figures 10(b), (c) and (e), under the combined action of spindle rotation motion, workpiece feed motion and ultrasonic vibration, the motion path of tool tip in 1D UVAM process is composed of hypocycloid and dense sawtooth line. Since ultrasonic machining is characterized by ultrasonic-frequency intermittent cutting mechanism, the tool tooth cutting trajectory is an important component of the tool motion trajectory. It can be obtained that the tool trajectory in UVAM is significantly changed compared to that in CM. Besides, Figures 10(d) and (f) illustrate the tool motion trajectory in UEVM process. It can be observed that the tool motion trajectory in UEVM is composed of hypocycloid and dense elliptic-like curve. Therefore, the applied direction of ultrasonic vibration and the dimension of ultrasonic vibration are essential to the tool motion trajectory in UVAM.

3.1.2 *Effect of Vibration Parameters and Cutting Parameters on Tool-Tip Trajectory*

In addition to the vibration direction and vibration dimension, ultrasonic vibration parameters and cutting parameters significantly influence the tool motion trajectory. Figure 11(a) shows the motion trajectory of the cutter teeth with an ultrasonic frequency of f = 40 kHz.

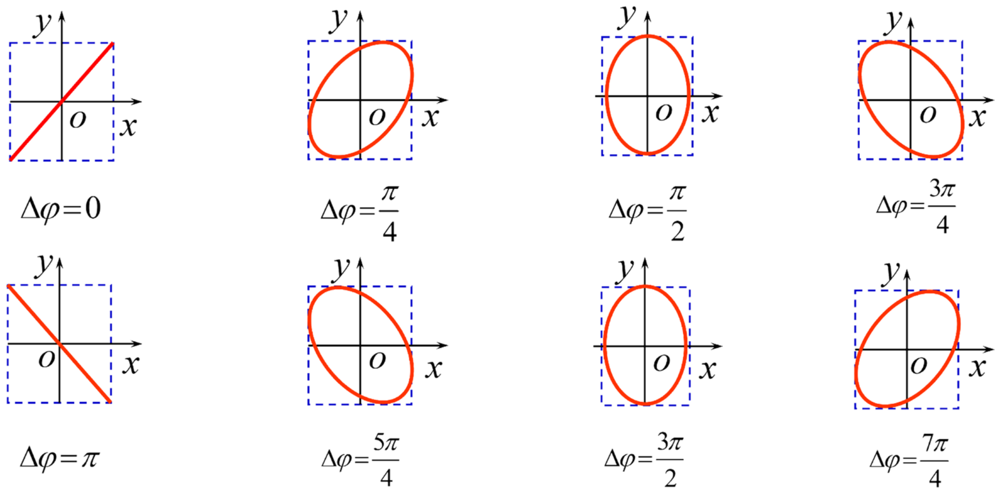

Figure 8 Effect of phase difference on the 2D elliptical shape in plane

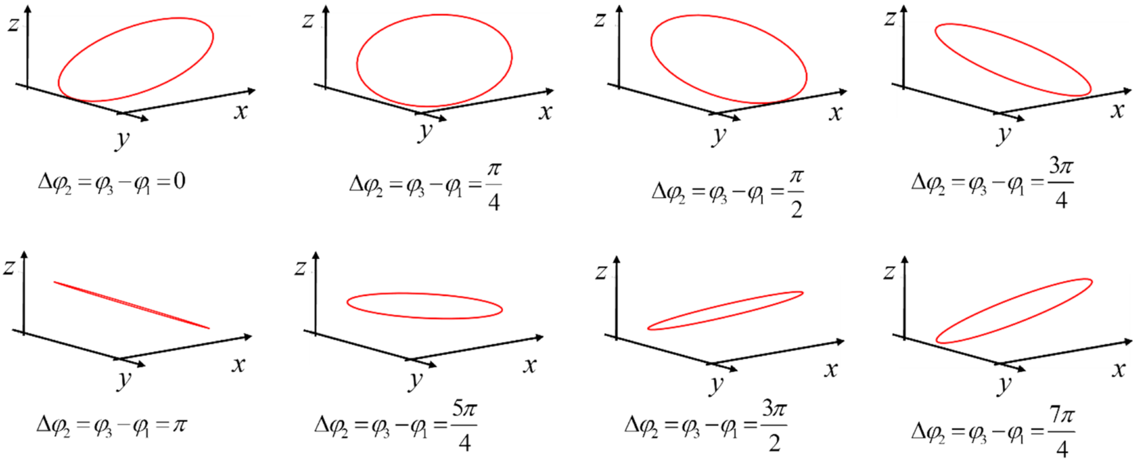

Figure 9 Effect of phase difference on the 3D elliptical shape in space

Compared with the tool trajectory in Figure 10(b), the density of the sawtooth curve and the overlap of the tool trajectory increase significantly as the ultrasonic frequency increases from 20 kHz to 40 kHz. Consequently, the density of the micro textures mapped onto the machined surface increases with the ultrasonic frequency. Besides, Figure 11(b) illustrates the tool trajectory with an ultrasonic amplitude of $A = 2$ μm. It can be obtained that the area of the overlapping region in the tool motion trajectory is significantly reduced due to the reduction of ultrasonic amplitude. The maximum vibration speed of the tool decreases with the decrease of the ultrasonic amplitude, where $v_{\max}=2\pi fA$. According to Ref. [29], the intermittent cutting evolves into continuous cutting when the maximum vibration speed is less than the cutting speed. Therefore, the size and density of the micro textures mapped on the machined surface decreased with decreasing ultrasonic amplitude.

Figure 11(c) illustrates the tool trajectory with a spindle speed of $N = 1200$ r/min. Compared with the tool trajectory in Figure 11(a), the density of the sawtooth curve in the tool trajectory significantly decreases in the y-direction as the spindle speed increases. From the perspective of the tool trajectory in UVAM, increasing the cutting speed has the effect of reducing ultrasonic vibration frequency. Therefore, relatively small cutting speeds are usually employed in ultrasonic machining to ensure the density of microtextures on machined surfaces. In addition, Figure 11(d) depicts the tool trajectory with a feed rate of $f = 16$ μm/z. Compared with the tool trajectory in Figure 11(b), increasing the feed rate can significantly reduce the overlapping area in the tool path. Obviously, the reduction of the overlapping area of tool trajectory will significantly reduce the density of the vibration texture on the machined surface in the feed direction. Therefore, the increase of the feed rate has the effect of reducing ultrasonic vibration amplitude to a certain extent. Thus, it is generally recommended that the tool feed per tooth is close to the ultrasonic amplitude to ensure the density of micro textures on machined surfaces.

3.2 Simulation of Microtextured Surface in UVAM

3.2.1 Validation of the Microtextured Surface Topography Model

The 1D UVAM experiments along the feed direction were performed to verify the effectiveness of the proposed microtextured surface topography prediction model. The machining trials were carried out on the vertical machining center TH 5650. The workpiece material is a typical difficult-to-machine material Ti–6Al–4V alloy, which is widely used in aerospace, biomedical and other critical areas. In the experiment and simulation, the feed rate, depth of cut, ultrasonic amplitude and ultrasonic frequency were 8 μm/z, 0.3 mm, 20 kHz and 10 μm, respectively. The tool radius is $d = 2$ mm, and the secondary declination of the tool is set to k'=5° in the simulation (the same below). The optical morphology and 3D topography of the machined surfaces were measured by the Keyence VHX microscope and STIL surface profiler Micromeasure 2. Figures 12(a) and 13(a) show the optical morphology of the machined surfaces at the spindle speed N=398 r/min and N=638 r/min, respectively. Accordingly, Figures 12(b) and 13(b) show the 3D topography of the machined surfaces at N=398 r/min and N=638 r/min, respectively. According to the prediction model and simulation flow chart of machined surface topography in UVAM, the predicted microtextured surface morphology at N=398 r/min and N=638 r/min are presented in Figures 12(c) and 13(c), respectively.

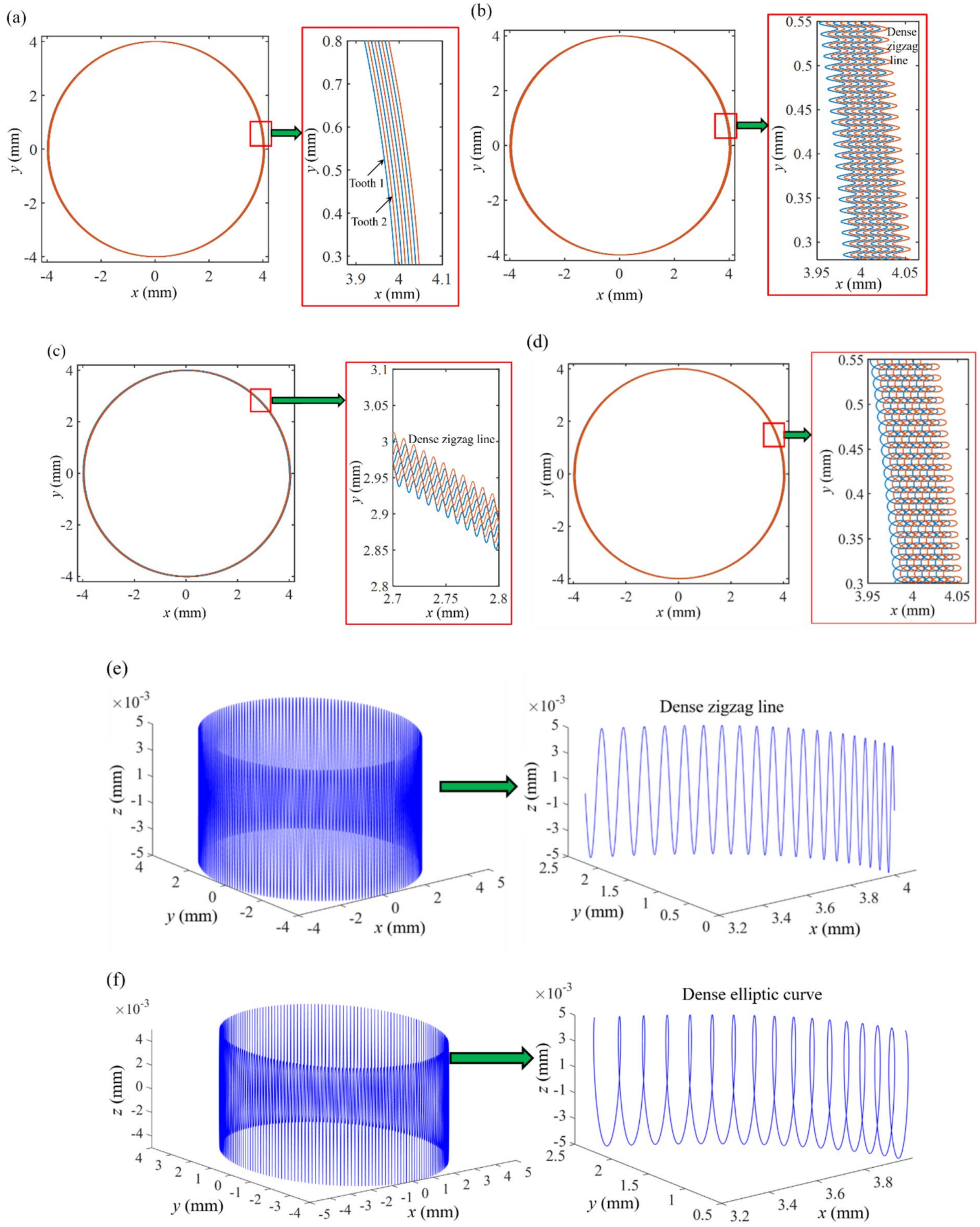

Figure 10 Tool-tip trajectory in different types of UVAM: **a** CM, **b** UVAM along the feed direction, **c** UVAM along the radial direction, **d** UEAM along the feed and radial directions, **e** UVAM along the axis direction, **f** UEAM along the feed and axis directions

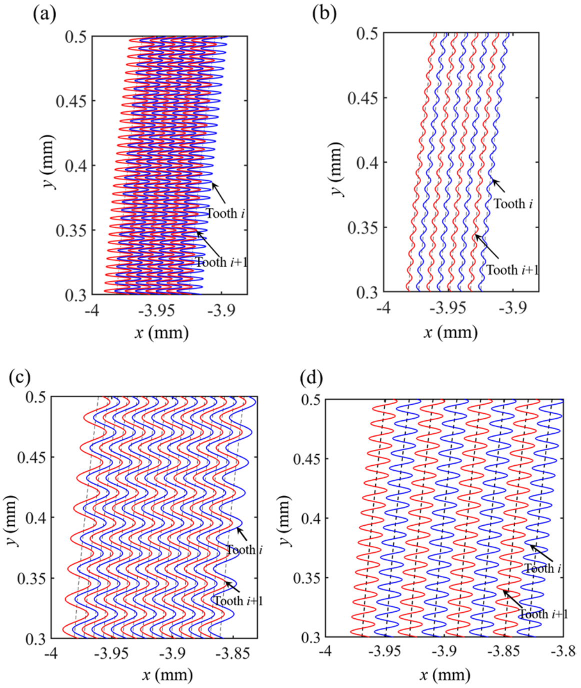

Figure 11 Effect of **a** ultrasonic frequency, **b** ultrasonic amplitude, **c** spindle speed and **d** feed rate on tool trajectory

By comparing the experimental and simulated surface morphology in Figures 12 and 13, it can be concluded that the developed surface morphology prediction model can effectively simulate the micro texture features on the machined surfaces. The uniformity of simulated micro textures is slightly better than that of the micro textures on the machined surfaces. This can be attributed to the negligence of the effects of cutting forces, cutting heat, machine accuracy and other factors on the surface topography during the simulation. Thus, the surface topography in the simulation is dominated by the sweeping trajectory of cutting edges, which mainly depends on tool geometry parameters, cutting parameters and vibration parameters. Moreover, Figures 12(d) and 13(d) show the simulated 3D surface topography after cubic spline interpolation. It can be observed that the transition between peaks and valleys on the simulated 3D surface topography becomes smoother after cubic spline interpolation. And the simulated 3D microtextured morphology is closer to the experimentally machined surface morphology in UVAM.

In addition to qualitatively comparing experimental and simulated surface topography, the quantitative comparison of the surface roughness is conducted to verify the accuracy of the proposed model. Thus, based on the statistics of the profile height values on the simulated surfaces, the surface roughness parameters *Ra* of microtextured surfaces can be calculated by Eq. (21).

$$Ra=\frac{1}{MN}\sum_{m=1}^{M}\sum_{n=1}^{N}\left|Hz(x_m,y_n)-\mu\right|, \tag{21}$$

where μ denotes the average height of the surface profile.

$$\mu=\frac{1}{MN}\sum_{m=1}^{M}\sum_{n=1}^{N}z(x_m,y_n). \tag{22}$$

According to Eqs. (21) and (22), the comparison of experimental and simulation results of the surface roughness *Ra* is shown in Figure 14. It can be obtained that the experimental results of surface roughness are larger than the simulation results. Simulation of machined surface topography is an ideal situation that only considers the effect of the geometry and motion trajectory of the tool on the machined surfaces. However, the machined surface topography is also influenced by a variety of other factors [30]. These factors can be broadly categorized as follows: Machine tool performance, tool performance, workpiece performance and the machining process. And each factor can be further subdivided into several subfactors. Therefore, relatively large errors appear in the experimental and predicted results of surface roughness. The prediction accuracy of roughness at medium speed (N=637 r/min) is higher than that at low speed (N=398 r/min), where the matching degree between the experimental and predicted results is about 72% at N=637 r/min. The relatively large error at N=398 r/min can be attributed to the relatively poor stability of the machine tool at low rotation speeds. In addition, the simulation results of surface roughness with and without interpolation are very close. Therefore, the simulation applying the third spline interpolation is more preferable to depict the microtextured surface topography in UVAM.

3.2.2 Effect of Tool Runout on Simulated Surface Topography

The tool runout of the machine Th5650 is measured using a laser displacement sensor M70LL/2 (virtins technology) with a high sampling frequency. As shown in Figure 15, the cylindrical part of the milling cutter was selected to measure the runout performance of the machine spindle because of the influence of milling cutter teeth on the measurement results. According to the principle of tool runout measurement illustrated in Figure 15(a), the linear relationship of tool runout values between the measurement position and the tool end can be expressed as Eq. (23):

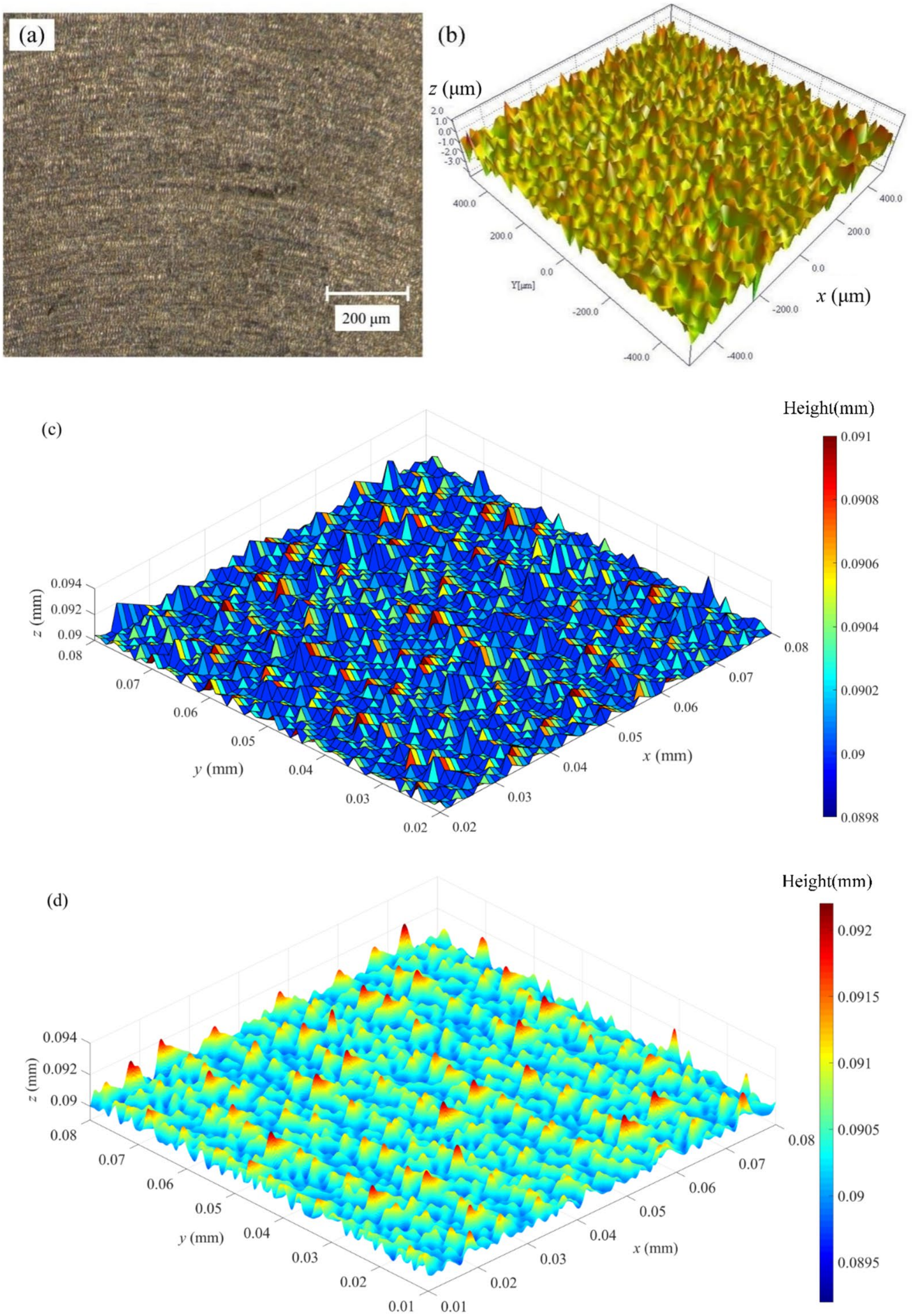

Figure 12 Comparison of experimental and simulated microtextured surface topography in UVAM at N=398 r/min: **a** 2D, **b** 3D machined surface topography, **c** 3D simulated surface topography, **d** 3D simulated surface topography after cubic spline interpolation

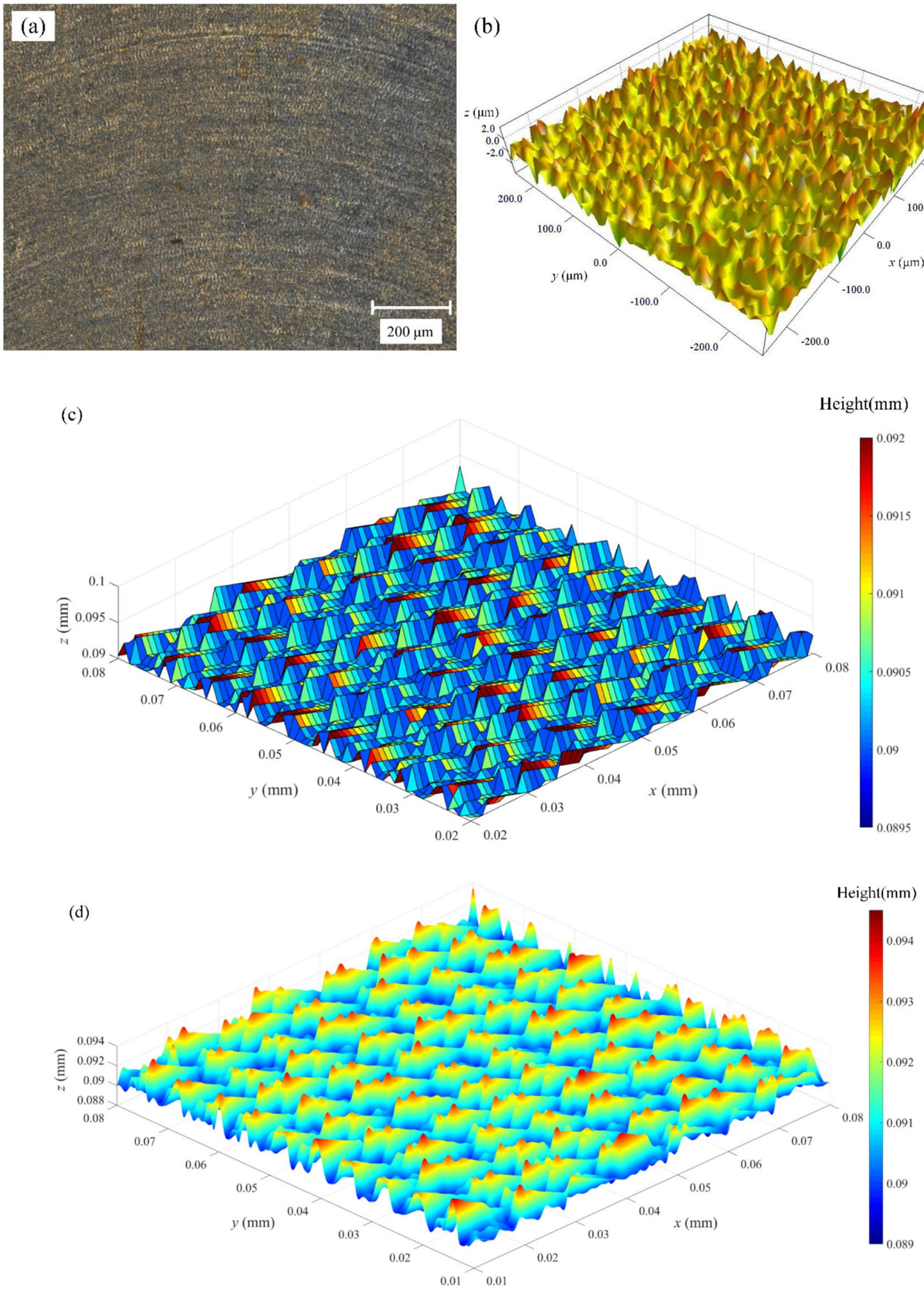

Figure 13 Comparison of experimental and simulated microtextured surface topography in UVAM at N=638 r/min: **a** 2D and **b** 3D machined surface topography, **c** 3D simulated surface topography and **d** 3D simulated surface topography after cubic spline interpolation

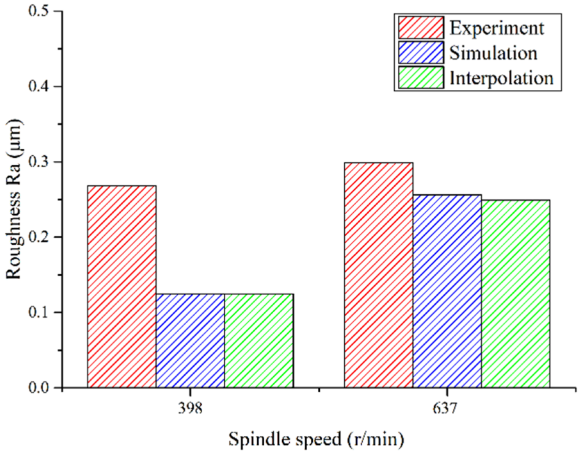

Figure 14 Comparison of experimental and simulation results of the surface roughness

$$y = -\frac{h}{\rho_c}x + H. \tag{23}$$

Thus, when y=0, the runout value at the end of the tool can be written as Eq. (24):

$$\rho_x = \frac{H\rho_c}{h}. \tag{24}$$

The influence of directional tool runout on simulated surface topography in UVAM is studied shown in Figure 16, where the runout value at the end of the tool is about ρ=40 μm. As shown in Figure 16(a), since the relatively large tool runout value, the tool runout in a certain direction has a large impact on the 3D surface topography during the initial machining stage. Accordingly, the microtextured morphology on the machined surfaces

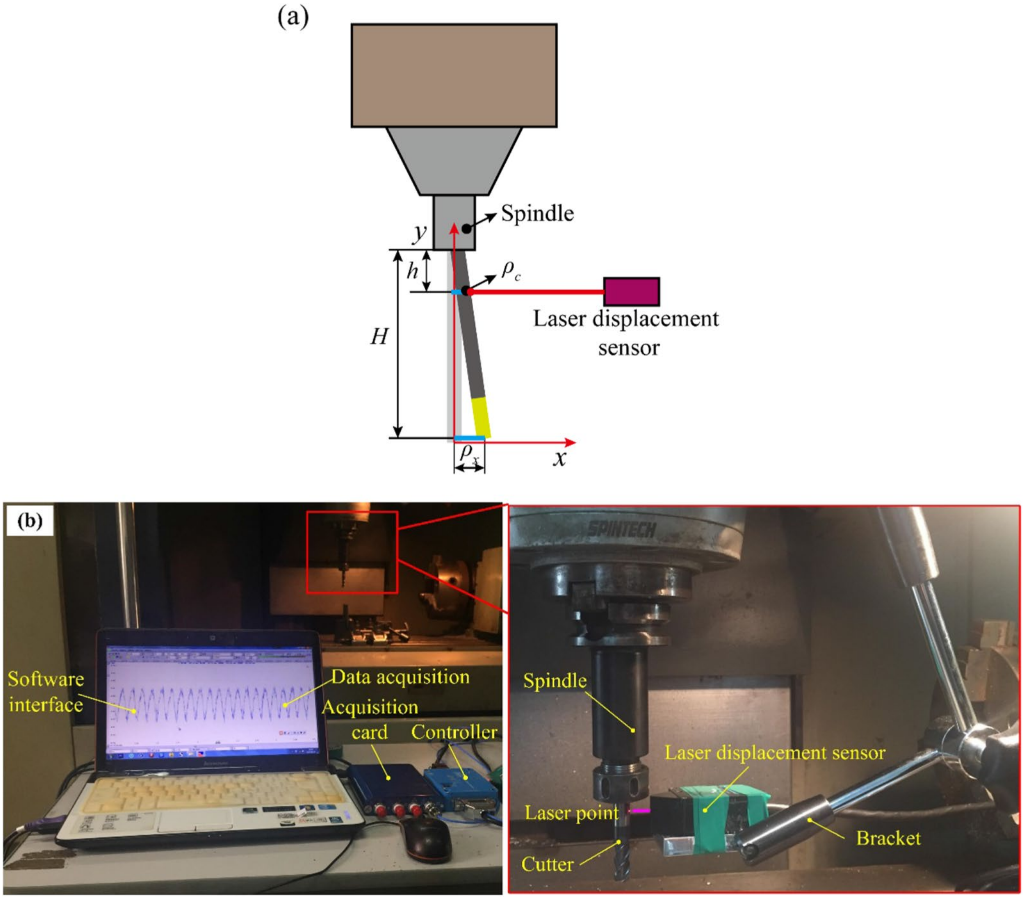

Figure 15 Tool runout measurement experiment: **a** Principle of tool runout measurement, **b** Tool runout measurement

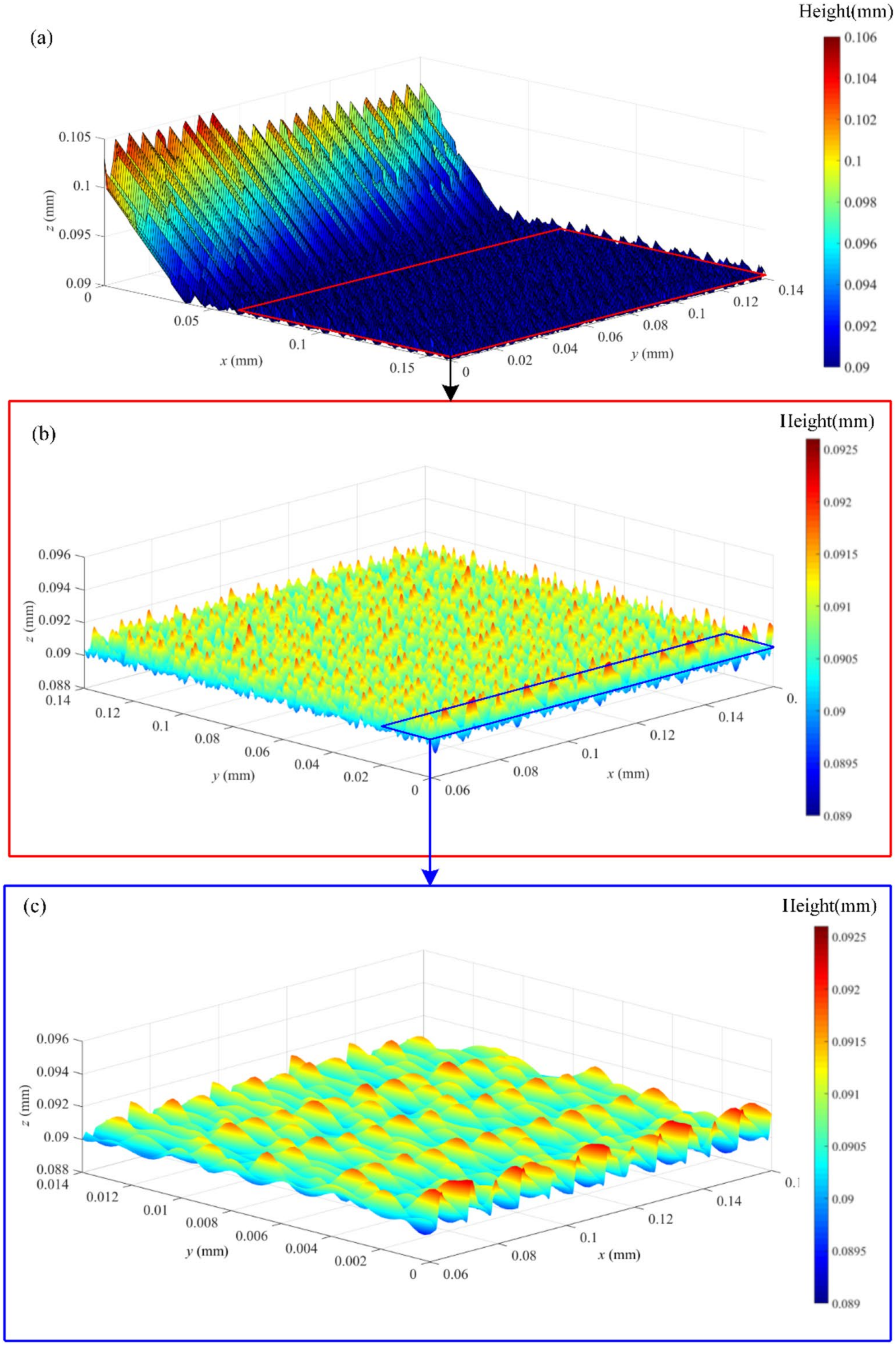

Figure 16 Effect of directional tool runout on microtextured surface topography in UVAM: **a** Overall 3D surface topography, **b** 3D surface morphology in the stable phase, **c** Enlarged view of microtextured surface

changes significantly. Figures 16(b) and (c) illustrate the simulated micro-texture surface morphology in the stable machining stage. It can be observed that dense and uniform micro texture occur on the machined surfaces during the stable machining stage. This is because the relatively high residual profile caused by tool runout is replaced by the subsequent lower tool sweep profile. Besides, the runout frequency of the spindle is very low compared to the ultrasonic vibration frequency. Therefore, the directional tool runout in a certain direction has less influence on the microtextured surface topography of machined surfaces in the stable machining stage.

3.2.3 Simulation of Microtextured Surface Topography

According to the established theoretical model, the prediction of 3D surface topography of microtextured surfaces machined by different types of UVAM systems is shown in Figure 17. The spindle speed and feed speed are N=600 r/min and f_z=8 μm/z, respectively. As shown in Figure 17(a), due to the presence of the secondary declination, the tooth feed trajectory with a significant height difference is a typical topography feature of conventional milling surfaces. Obviously, these undulating toolpaths are the primary cause for the reduction of surface quality in general milling. Figure 17(b) presents the microtextured surface morphology characteristics in the feed-direction UVAM process, where the ultrasonic frequency and amplitude are f=20 kHz and A_x=10 μm, respectively. Compared with the surface topography in general milling, the highly fluctuating tooth trajectory on the machined surface is replaced by the dense micro textures with low fluctuation under the action of ultrasonic vibration.

The simulation of microtextured surface topography in rotary UVAM system is shown in Figure 17(c), where the ultrasonic frequency and amplitude are f=20 kHz and A_z=10 μm, respectively. Since the ultrasonic vibration along the tool axis has a greater effect on the depth of cut and less effect on the cutting trajectory in the horizontal plane. Consequently, distinct toolpaths are still present on the 3D surface morphology in rotary UVAM process. Besides, the height fluctuation of tooth feed trajectory obtained by rotary UVAM is greater than that of tooth feed trajectory produced by conventional milling due to the axial ultrasonic vibration. Figure 17(d) illustrates the simulated surface topography produced by UEVAM in horizontal plane, where the ultrasonic amplitudes in the x (feed-direction) and y directions are A_x=10 μm and A_y=6 μm, respectively. Compared with the micro textures on the surfaces machined by 1D UVAM, the uniformity and denseness of the micro textures on the surfaces produced by UEVAM in horizontal plane are improved.

Figure 17(e) shows the simulated surface topography obtained by UEVAM system in vertical plane, where the ultrasonic amplitudes in the x (feed-direction) and z directions are A_x=10 μm and A_z=6 μm, respectively. Compared to the surface morphology machined by 1D rotary UVAM shown in Figure 17(c), the height fluctuation of tooth feed trajectory obtained by rotary UEVAM is significantly reduced. However, since the ultrasonic vibration direction is the same as the cutting depth direction, the height fluctuation of tooth feed trajectory in rotary UEVAM process is still greater than that of tooth feed trajectory in normal milling. Finally, the simulation of microtextured surface morphology machined by 3D UEVAM system is shown in Figure 17(f), where the ultrasonic amplitudes in the x, y and z directions are A_x=10 μm, A_y=6 μm and A_z=6 μm, respectively. It can be observed that distinct ellipsoidal craters appear on 3D UEVAM machined surface.

3.2.4 Prediction of Surface Roughness

According to Eqs. (21) and (22), the prediction of surface roughness Ra of microtextured surfaces fabricated by different types of UVAM systems is given in Figure 18, where the simulation parameters used in surface roughness prediction are the same as those in surface topography prediction in Section 3.2.3. As shown in Figure 18, the surface roughness produced by 1D feed-direction UVAM and 2D UEVAM in horizontal plane is superior to that of conventional milling surface. However, the surface roughness produced by 1D rotary UVAM is much higher than that produced by other methods. This is mainly attributed to the fact that the direction of the applied ultrasonic vibration is the same as the cutting depth direction. In addition, the relatively large vibration amplitude (A_z=10 μm) is also an important factor affecting the fluctuation of tooth feed trajectory. In addition, due to the existence of ultrasonic amplitude component along the cutting depth, the surface roughness obtained by 2D and 3D UEVAM in the vertical plane is higher than that obtained by normal milling.

4 Conclusions

Based on the theoretical modeling and roughness prediction of microtextured surfaces processed by different types of UVAM systems, the following conclusions can be drawn.

(1) From the perspective of tool trajectories, increasing the cutting speed and feed rate has the effect of reducing ultrasonic frequency and ultrasonic amplitude to a certain extent, respectively. The results indicate that low cutting speeds, low feed rates and low axial ultrasonic amplitudes are benefi-

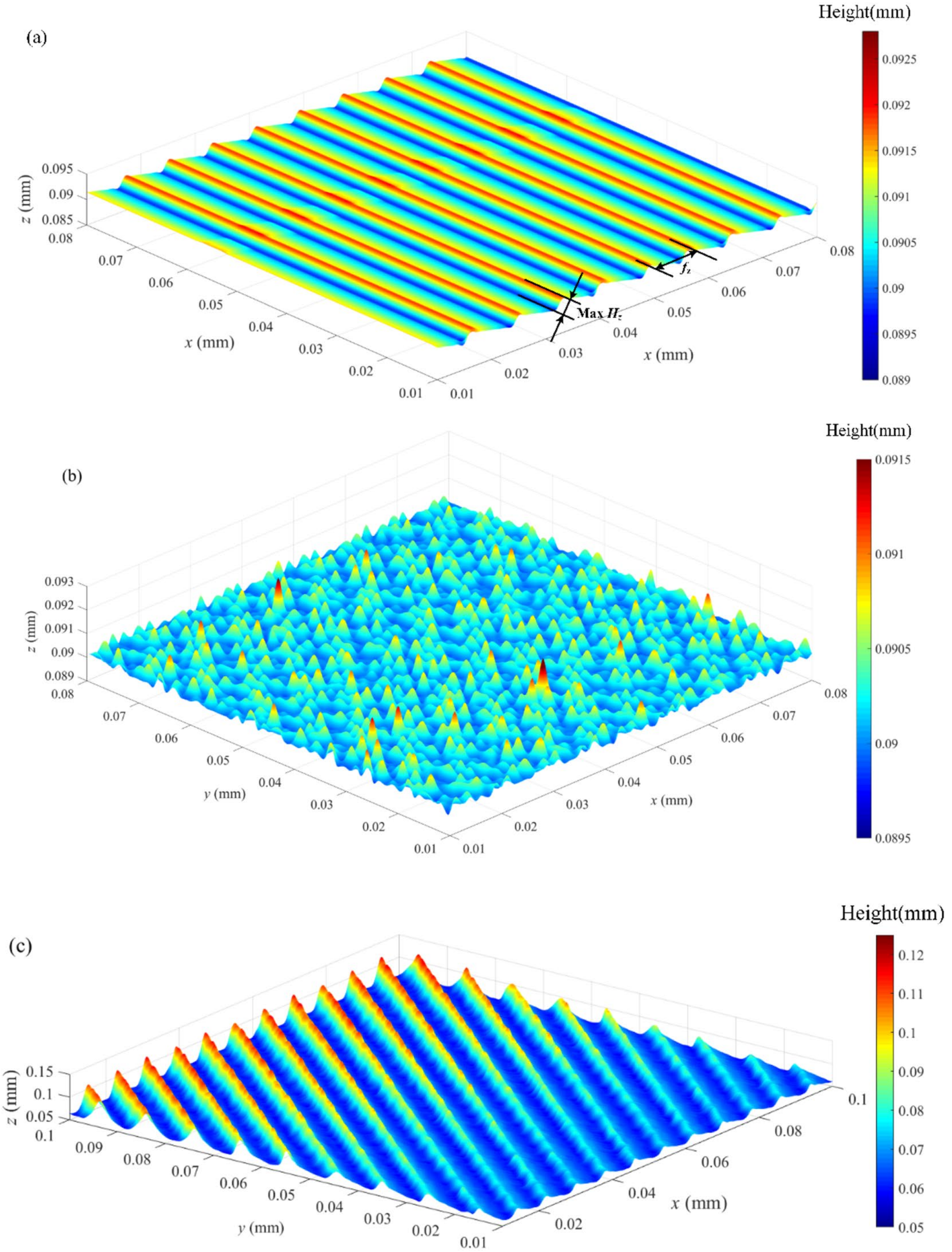

Figure 17 Simulation of 3D surface topography in different types of UVAM **a** General milling, **b** 1D UVAM along the feed direction, **c** 1D UVAM along the tool axis direction, **d** 2D UVAM in horizontal plane, **e** 2D UVAM in vertical plane and **f** 3D UVAM in space

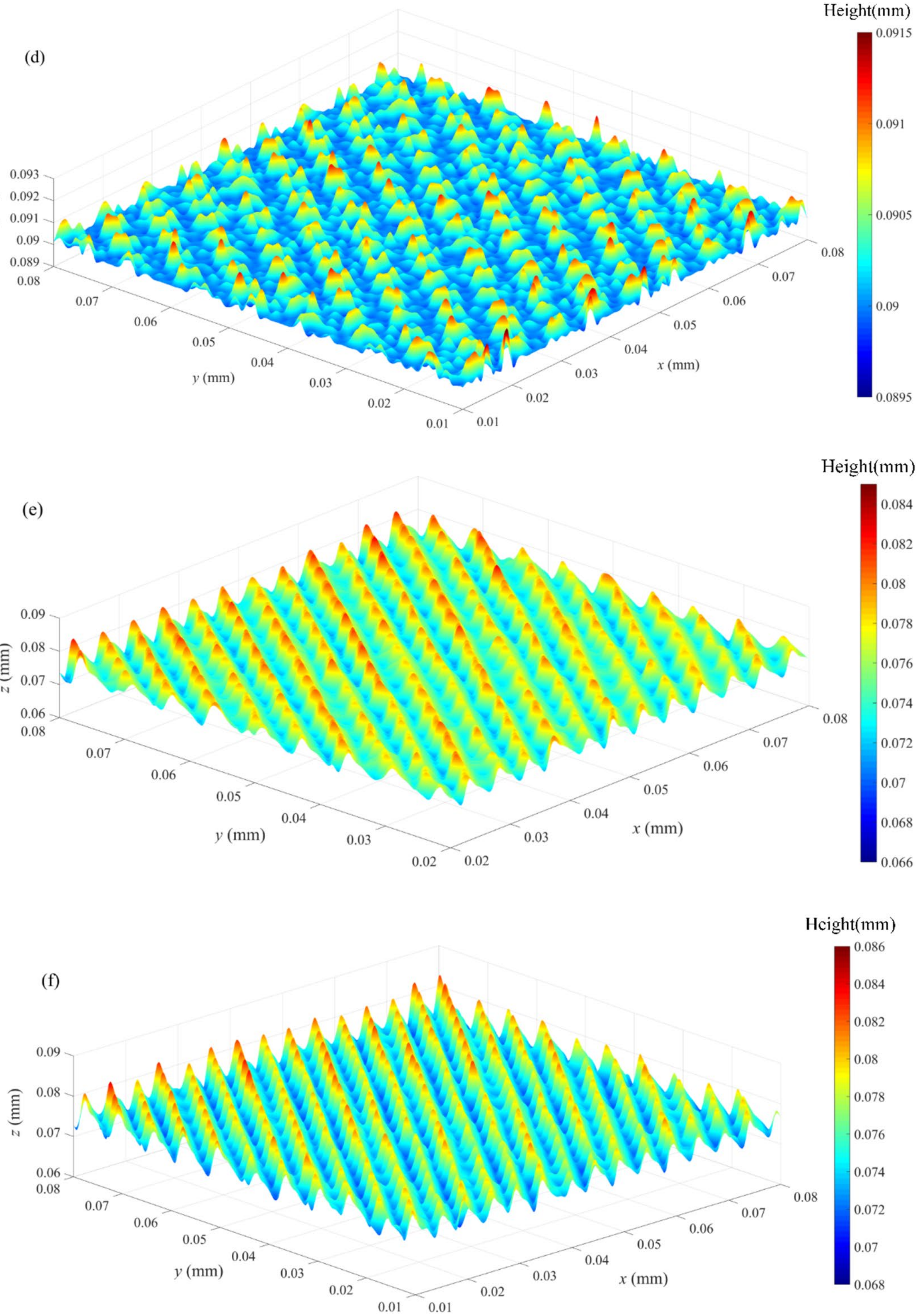

Figure 17 continued

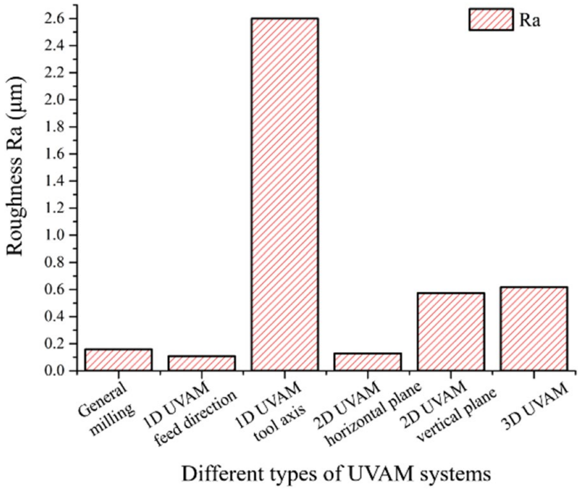

Figure 18 Prediction and comparison of the surface roughness in different types of UVAM process

cial to improve the micro-texture distribution and roughness of the machined surfaces in UVAM.

(2) The simulation model with cubic spline interpolation is more suitable for characterizing the distribution and geometric features of microtextured surfaces than the conventional simulation model due to the presence of numerous micro textures. Due to the poor stability of the machine tool at low rotation speeds, the prediction accuracy of roughness at medium speed (N=637 r/min) is higher than that at low speed (N=398 r/min).

(3) Compared with uniform microtextured surfaces machined by 1D feed-direction UVAM and 2D UEVAM in horizontal plane, obvious tooth trajectory with large height fluctuation is one of typical topography features of the surfaces processed by 1D rotary UVAM, 2D and 3D UEVAM in vertical plane.

(4) The surface roughness of microtextured surfaces obtained by 1D feed-direction UVAM and 2D UEVAM in horizontal plane is superior to that of conventional milling surfaces, while the surface roughness produced by 1D rotary UVAM, 2D and 3D UEVAM in vertical plane is inferior to that of conventional milled surfaces.

Acknowledgements
Not applicable.

Authors' Contributions
CN proposed the idea and wrote the manuscript; JZ, DL and XW assisted with sampling and laboratory analyses; YW and LZ assisted with manuscript revision. All authors read and approved the final manuscript.

Funding
Supported by Shandong Provincial Natural Science Foundation of China (Grant No. ZR2023QE041), China Postdoctoral Science Foundation (Grant No. 2023M731862), National Natural Science Foundation of China (Grant No. 51975112).

Data availability
The authors are grateful to Prof. Lida Zhu of Northeastern University for his guidance and assistance in this study.

Declarations

Competing Interests
The authors declare no competing financial interests.

Received: 20 April 2023 Revised: 2 April 2024 Accepted: 11 April 2024

References

[1] Z Yang, L Zhu, G Zhang, et al. Review of ultrasonic vibration-assisted machining in advanced materials. *International Journal of Machine Tools and Manufacture*, 2020, 156: 103594.
[2] J Zhang, T Cui, C Ge, et al. Review of micro/nano machining by utilizing elliptical vibration cutting. *International Journal of Machine Tools and Manufacture*, 2016, 106: 109-126.
[3] A Arslan, H H Masjuki, M A Kalam, et al. Surface texture manufacturing techniques and tribological effect of surface texturing on cutting tool performance: A review. *Critical Reviews in Solid State and Materials Sciences*, 2016, 41: 447-481.
[4] A Kumar, S C Sharma. Textured conical hybrid journal bearing with ER lubricant behavior. *Tribology International*, 2019, 129: 363-376.
[5] T Chang, Z Guo, C Yuan. Study on influence of Koch snowflake surface texture on tribological performance for marine water-lubricated bearings. *Tribology International*, 2019, 129: 29-37.
[6] J Michalski, L Skoczylas. A comparative analysis of the geometrical surface texture of a real and virtual model of a tooth flank of a cylindrical gear. *Journal of Materials Processing Technology*, 2008, 204: 331-342.
[7] J Jiang, W Zhao, X Peng, et al. A novel design for discrete surface texture on gas face seals based on a superposed groove model. *Tribology International*, 2020, 147: 106269.
[8] T Özel, D Biermann, T Enomoto, et al. Structured and textured cutting tool surfaces for machining applications. *CIRP Annals*, 2021, 70: 495-518.
[9] Z Sun, D Geng, W Zheng, et al. An innovative study on high-performance milling of carbon fiber reinforced plastic by combining ultrasonic vibration assistance and optimized tool structures. *Journal of Materials Research and Technology*, 2023, 22: 2131-2146.
[10] M Vishnoi, P Kumar, Q Murtaza. Surface texturing techniques to enhance tribological performance: A review. *Surfaces and Interfaces*, 2021, 27: 101463.
[11] W Wang, Q Guo, Z Yang, et al. A state-of-the-art review on robotic milling of complex parts with high efficiency and precision. *Robotics and Computer-Integrated Manufacturing*, 2023, 79: 102436.
[12] X Shen, G Tao, Tribological behaviors of two micro textured surfaces generated by vibrating milling under boundary lubricated sliding. *International Journal of Advanced Manufacturing Technology*, 2015, 79: 1995-2002.
[13] G Tao, C Ma, L Bai, et al. Feed-direction ultrasonic vibration—assisted milling surface texture formation. *Materials and Manufacturing Processes*, 2017, 32: 193-198.
[14] S Amini, H N Hosseinabadi, S A Sajjady. Experimental study on effect of micro textured surfaces generated by ultrasonic vibration assisted face turning on friction and wear performance. *Applied Surface Science*, 2016, 390: 633-648.
[15] H N Hosseinabadi, S A Sajjady, S Amini. Creating micro textured surfaces for the improvement of surface wettability through ultrasonic vibration assisted turning. *The International Journal of Advanced Manufacturing Technology*, 2018, 96: 2825-2839.

[16] P Guo, Y Lu, K F Ehmann, et al. Generation of hierarchical micro-structures for anisotropic wetting by elliptical vibration cutting. *CIRP Annals*, 2014, 63: 553-556.
[17] S Xu, K Shimada, M Mizutani, et al. Analysis of machinable structures and their wettability of rotary ultrasonic texturing method. *Chinese Journal of Mechanical Engineering*, 2016, 29: 1187-1192.
[18] Z Chen, P Feng, J Zhang, et al. Shaped vibration cutting: A novel fabrication method for mid-infrared relief gratings with controllable profiles. *Journal of Materials Processing Technology*, 2023, 317: 118007.
[19] X Liu, M Soshi, A Sahasrabudhe, et al. A geometrical simulation system of ball end finish milling process and its application for the prediction of surface micro features. *Journal of Manufacturing Science and Engineering*, 2005, 128: 74-85.
[20] Y Sun, Z Shi, Q Guo, et al. A novel method to predict surface topography in robotic milling of directional plexiglas considering cutter dynamical displacement. *Journal of Materials Processing Technology*, 2022, 304: 117545.
[21] X Liu, D Wu, J Zhang, et al. Analysis of surface texturing in radial ultrasonic vibration-assisted turning. *Journal of Materials Processing Technology*, 2019, 267: 186-195.
[22] J Jiang, S Sun, D Wang, et al. Surface texture formation mechanism based on the ultrasonic vibration-assisted grinding process. *International Journal of Machine Tools and Manufacture*, 2020, 156: 103595.
[23] Z Yang, L Zhu, C Ni, et al. Investigation of surface topography formation mechanism based on abrasive-workpiece contact rate model in tangential ultrasonic vibration-assisted CBN grinding of ZrO2 ceramics. *International Journal of Mechanical Sciences*, 2019, 155: 66-82.
[24] L Zhu, C Ni, Z Yang, et al. Investigations of micro-textured surface generation mechanism and tribological properties in ultrasonic vibration-assisted milling of Ti–6Al–4V. *Precision Engineering*, 2019, 57: 229-243.
[25] C Ni, L Zhu, C Liu, et al. Analytical modeling of tool-workpiece contact rate and experimental study in ultrasonic vibration-assisted milling of Ti–6Al–4V. *International Journal of Mechanical Sciences*, 2018, 142: 97-111.
[26] H Lu, L Zhu, Z Yang, et al. Research on the generation mechanism and interference of surface texture in ultrasonic vibration assisted milling. *International Journal of Mechanical Sciences*, 2021, 208: 106681.
[27] S Qin, L Zhu, M Wiercigroch, et al. Material removal and surface generation in longitudinal-torsional ultrasonic assisted milling. *International Journal of Mechanical Sciences*, 2022, 227: 107375.
[28] Y Liu, D Zhang, D Geng, et al. Ironing effect on surface integrity and fatigue behavior during ultrasonic peening drilling of Ti-6Al-4 V. *Chinese Journal of Aeronautics*, 2023, 36(5): 486-498.
[29] C Nath, M Rahman. Effect of machining parameters in ultrasonic vibration cutting. *International Journal of Machine Tools and Manufacture*, 2008, 48(9): 965-974.
[30] Q Guo, W Wang, Y Jiang, et al. 3D surface topography prediction in the five-axis milling of plexiglas and metal using cutters with non-uniform helix and pitch angles combining runout. *Journal of Materials Processing Technology*, 2023, 314: 117885.

Chenbing Ni born in 1989, is currently an associate professor at *Qingdao University of Technology, China*. He received his PhD degree from *Northeastern University, China*, in 2021. His research interests include ultrasonic machining and additive/subtractive hybrid manufacturing.

Junjie Zhu born in 1999, is currently a master candidate at *Qingdao University of Technology, China*. His research interests focus on precision grinding and additive/subtractive hybrid manufacturing.

Youqiang Wang born in 1970, is currently a professor at *Qingdao University of Technology, China*. His research interests include tribology and surface interface engineering.

Dejian Liu born in 1994, is currently a PhD candidate at *Qingdao University of Technology, China*. His research interests include precision machining and additive/subtractive hybrid manufacturing.

Xuezhao Wang born in 1994, is currently a PhD candidate at *Qingdao University of Technology, China*. His research interests focus on processing of magnesium alloys.

Lida Zhu born in 1979, is currently a professor at *Northeastern University, China*. His research interests include precision machining, ultrasonic machining and additive/subtractive hybrid manufacturing.